Ionic and Charge Carrier Transport Properties of Twin Domains in Halide Perovskites

Jae Sung Yun[¶,*,1,2], Dohyung Kim[¶,3,10], Arun Sagotra[3], Alessandro Mattoni[4], Pankaj Sharma[3,9], Jincheol Kim[6], Dasuel Lee[1], Sean Lim[7], Padraic O'Reilly[8], Liz Brinkman[8], Martin A. Green[1], Shujuan Huang[6], Anita Ho-Baillie[1], Claudio Cazorla[4], and Jan Seidel[3,10*]

[1] Australian Centre for Advanced Photovoltaics (ACAP), School of Photovoltaic and Renewable and Engineering, University of New South Wales, Sydney 2052, Australia

[2]Department of Electrical and Electronic Engineering, Advanced Technology Institute (ATI), University of Surrey, Guildford GU2 7XH, UK

[3] School of Materials Science and Engineering, University of New South Wales, Sydney 2052, Australia

[4]Department de Física, Universitat Politècnica de Catalunya, Campus Nord B4-B5, Barcelona, E-08034 Spain

[5] Consiglio Nazionale delle Ricerche, Istituto Officina dei Materiali, CNR-IOM, Cittadella Universitaria, Monserrato 09042-I, Cagliary, Italy

[6] School of Engineering, Macquarie University, Sydney, New South Wales, 2109 Australia

[7] Electron Microscopy Unit, University of New South Wales, Sydney 2052, Australia

[8] Molecular Vista, San Jose, CA 95119, USA

[9] ARC Centre of Excellence in Future Low-Energy Electronics Technologies (FLEET), UNSW Sydney, Sydney 2052, Australia

[10] Photovoltaics Laboratory, Korea Institute of Energy Research, Daejeon 34129, Republic of Korea

†Correspondence: j.yun@unsw.edu.au, jan.seidel@unsw.edu.au
¶These authors contributed equally.

Abstract

The past decade has seen the unprecedentedly rapid emergence of a new class of solar cells based on mixed organic–inorganic halide perovskites. The power conversion efficiency (PCE) of halide perovskite solar cells since then has quickly risen above 25% in single-junction devices and 30% in tandem devices. Twin domains within polycrystalline grains have been recently reported in this material, nevertheless, their roles associated with both ionic and charge carrier transport properties are still to be fully understood. Here, combining molecular dynamic (MD) simulations with nanoscale scanning probe microscopy investigations, we reveal unique properties of the twin domains that exhibit vital channels for ion migration and influence charge separation and collection. Our nanoscale elemental analysis using photo-induced force microscopy reveals that the domain structure possesses an alternating chemical compositional variation, rich and poor in cations for low topography domains (LTDs) and high topography

domains (HTDs) respectively. Also, Kelvin probe force microscopy (KPFM) measurements confirm that LTDs provide a confined tunnel for cation vacancy migration. This phenomenon is supported by the MD simulation which suggests the presence of the twin domain wall causes a reduction in the crystal symmetry and appearance of a strain field. Lastly, KPFM and conductive AFM (c-AFM) under illumination show that both photovoltage and photocurrent are higher at LTDs due to the effective charge collection by ion accumulation. This work highlights important elements of the nanoscale intragrain feature that may pave the way to high-efficiency perovskite solar cells.

Introduction

Organometal halide perovskites (OHPs) have emerged as an outstanding optoelectronic material for various applications such as photovoltaics[1, 2], photodectors[3], radiation detectors[4] and light-emitting diodes[5]. In particular, tremendous improvement in the photoconversion efficiency of solar cells has been achieved within the short time of their development, from 3.8% in 2007 to a recent certified record over 25.7%.[6] This is primarily owing to the superior optoelectronic properties of OHP solar cells such as high optical absorption coefficient, tunable bandgap, long carrier diffusion length, defect-tolerance, and high ambipolar charge carrier mobility.[7, 8, 9, 10, 11] OHP films prepared by using the solution or vapor processes are polycrystalline in nature and possess various types of structural defects such as grain boundaries, twin boundaries, and point defects that result in both structural and electrical inhomogeneity. Local electronic and structural characterization techniques have revealed that these defects cause facet-dependent charge transport properties[12, 13], halide segregation[14], ion migration through grain boundaries[15, 16], and local strain and bandgap inhomogeneity[17, 18]. The effect of these defects on overall solar cell performance is significant[19, 20], and a detailed understanding is vital for further developments.

Previously, we reported that grain boundaries in $MAPbI_3$ films exhibit beneficial effects in terms of charge transport properties.[14] Later, we explored mixed cation and halide perovskites and reported that the grain boundaries are preferential channels for ion migration.[15, 21] This property arises due to the structural properties of the grain boundaries which have a lack of chemical bonding, thus providing a larger open space for ion migration compared to the grain interiors.[22] Accordingly, the activation energy of ion migration at the grain boundaries is expected to be lower than in the grain interior.[23] Recently, another important type of nanoscale structural defect, *i.e.* ferroelastic twin domains, has attracted significant attention in both single composition ($MAPbI_3$) and mixed perovskites. These domains have lateral spacings between 40-350 nm and exist within individual grains of the halide perovskites films and single crystals, as revealed by piezoresponse force microscopy (PFM) and transmission electron microscopy (TEM).[24, 25, 26, 27, 28, 29] OHPs in the tetragonal phase can have six crystallographic orientation states, which can manifest in ferroic stripe domains.[30] Rothmann *et al*[25] reported that these domains are appearing and disappearing upon cooling/heating in a reversible process at the cubic-to-tetragonal phase transition temperature (approximately 57 °C). Therefore, it was suspected that the domain formation is due to the appearance of spontaneous strain associated with the tetragonal state at the phase transition. This evidence on the existence of twin domains has led to the examination of various associated optoelectronic and material properties. It was shown that the domains have variations of the electrical and electromechanical properties due to alternating high and low methylammonium concentration in $MAPbI_3$ perovskite[21] and that these domains have minor impact on the photoluminescence behavior.[31] Another interesting point has been raised by the same group, namely that twin domains can affect ionic mobility and confine ion diffusion.[32] The twin domain pattern was also observed in mixed perovskite films of $(FAPbI_3)_{0.85}(MAPbBr_3)_{0.15}$, which has been reported by our group. It was shown that light and bias can induce structural modulation of the domain structure.[13] Recently, a negligible influence on electronic transport properties of the twin walls (TWs) in single crystal $MAPbI_3$

perovskite has been reported.[31] On the other hand, others argue that ferroelastic twin domains heavily influence charge carrier diffusion in $MAPbI_3$.[33] Therefore, further work is required regarding the relationship between charge carrier transport and twin domain structures, and their correlation with optoelectronic properties of OHPs.

In this work, we use both theoretical and experimental methods to investigate the properties of the domain structure and overall material system. Using photo-induced force microscopy (PiFM), we discover the topographical facet of the domain pattern, alternating high and low topography heights, which features both MA and FA cation compositional variance. Our bias voltage dependent Kelvin probe force microscopy (KPFM) reveals that the low topography domains (LTDs) are channels for ion migration, thus, promoting the overall increase of ion migration of the domain system. This observation is supported by molecular dynamics (MD) simulations which suggest that iodide ion diffusivity is enhanced by a factor of 2.4 in the twin domain system compared to a single domain system. This is owing to a breaking of crystal symmetries at the ferroelastic TWs when an electric-field is applied to the system. Furthermore, we examine charge separation and collection properties of the domain system using KPFM and conductive atomic force microscopy (c-AFM) under illumination. Our results highlight the unique nanoscale charge transport properties of the twin domain system that can influence the device performance.

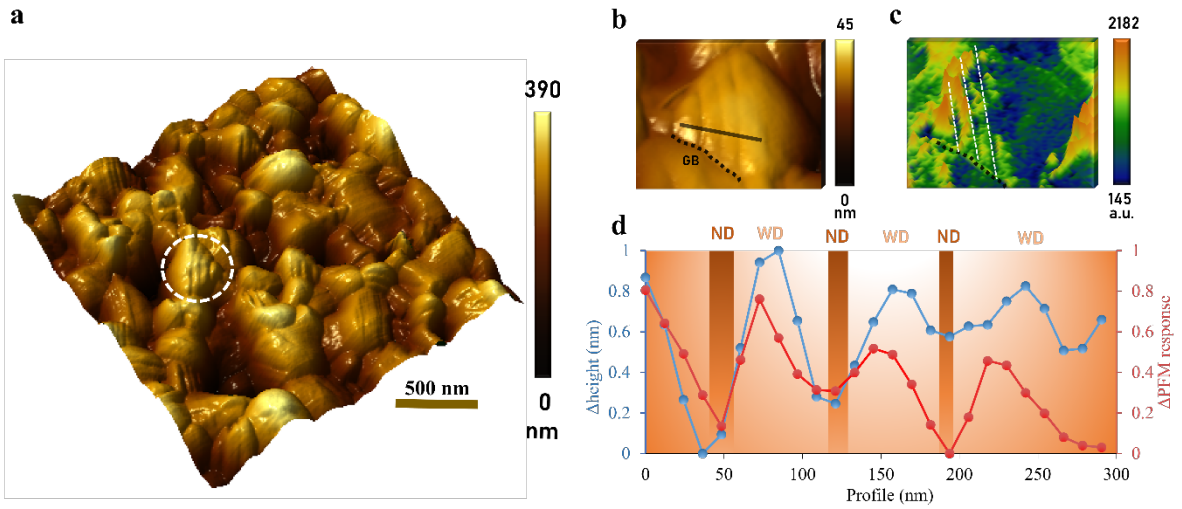

Fig. 1. Twin domain patterns in a $(FAPbI_3)_{0.85}(MAPbBr_3)_{0.15}$ film. a. 3D AFM topography image (2 x 2 μm). **b**. Magnified 3D topography image (White circle in (a) and GB denotes grain boundary) and **c.** Corresponding PFM amplitude image. **d.** Change in height and out-of-plane piezo-response amplitude profiles (averaged line profiles in (b) and (c)) where ND and WD represent narrow domain and wide domain, respectively.

Firstly, we consider the microstructural features of domains in the perovskite. We adopted a compositional engineered OHP in the form of $(FAPbI_3)_{0.85}(MAPbBr_3)_{0.15}$, which has been shown to be one of the most effective ways to realize record-efficiency perovskite solar cells. The structure of the samples consists of a FTO/c-TiO_2/m-TiO_2/$(FAPbI_3)_{0.85}(MAPbBr_3)_{0.15}$ configuration that ensures device-relevant morphological and associated electronic functionality. The solar cell architecture and the perovskite composition used in this study results in typical power conversion efficiencies of 18-20% when a full device structure is made using Spiro-MeOTAD as a hole transport material and gold contacts.[34] A typical *J-V* characteristic of the device is shown in Fig. S1a. X-ray diffraction (XRD) data of the perovskite layer is displayed in Fig. S1b which reveals strong (110) crystal orientation. All experiments are carried out under ambient conditions with a relative humidity of 30-40% and consistent and repetitive results could be demonstrated. Note that the composition used in our study is significantly stable under ambient air and does not degrade during our measurements.

Fig. 1 shows the 3D AFM topography of the sample surface. There are some grains that have stripe-like corrugated features corresponding to ferroelastic domains. We have previously reported that such domains can be structurally modulated under electrical bias and light.[35] A magnified image of a single perovskite grain with periodic domains is shown in Fig. 1b and the corresponding piezo-response amplitude image is shown in Fig. 1c. To investigate the topological structure of the domains, line profiles (see Fig. 1d) in height and amplitude are obtained from Fig. 1b-c. From this profile, there is an alternating wide (60-80nm) and narrow (10-20nm) domain pattern. From our previous report, the domains in the mixed perovskite are generated from the cubic to tetragonal phase transition during the cooling process of the material.[35] The phase transition is accompanied by a loss of translational symmetry, resulting

in the formation of twin domains or antiphase domains.[36] We notice that an alternating PFM amplitude variation (Fig. 1c) follows the topographical feature of the domain pattern. As can be seen, a wave pattern consisting of low topography domains (LTDs) and high topography domains (HTDs) are visible from the height profile (Fig. 1d) and the corresponding amplitude at LTDs is always lower compared to the HTDs.

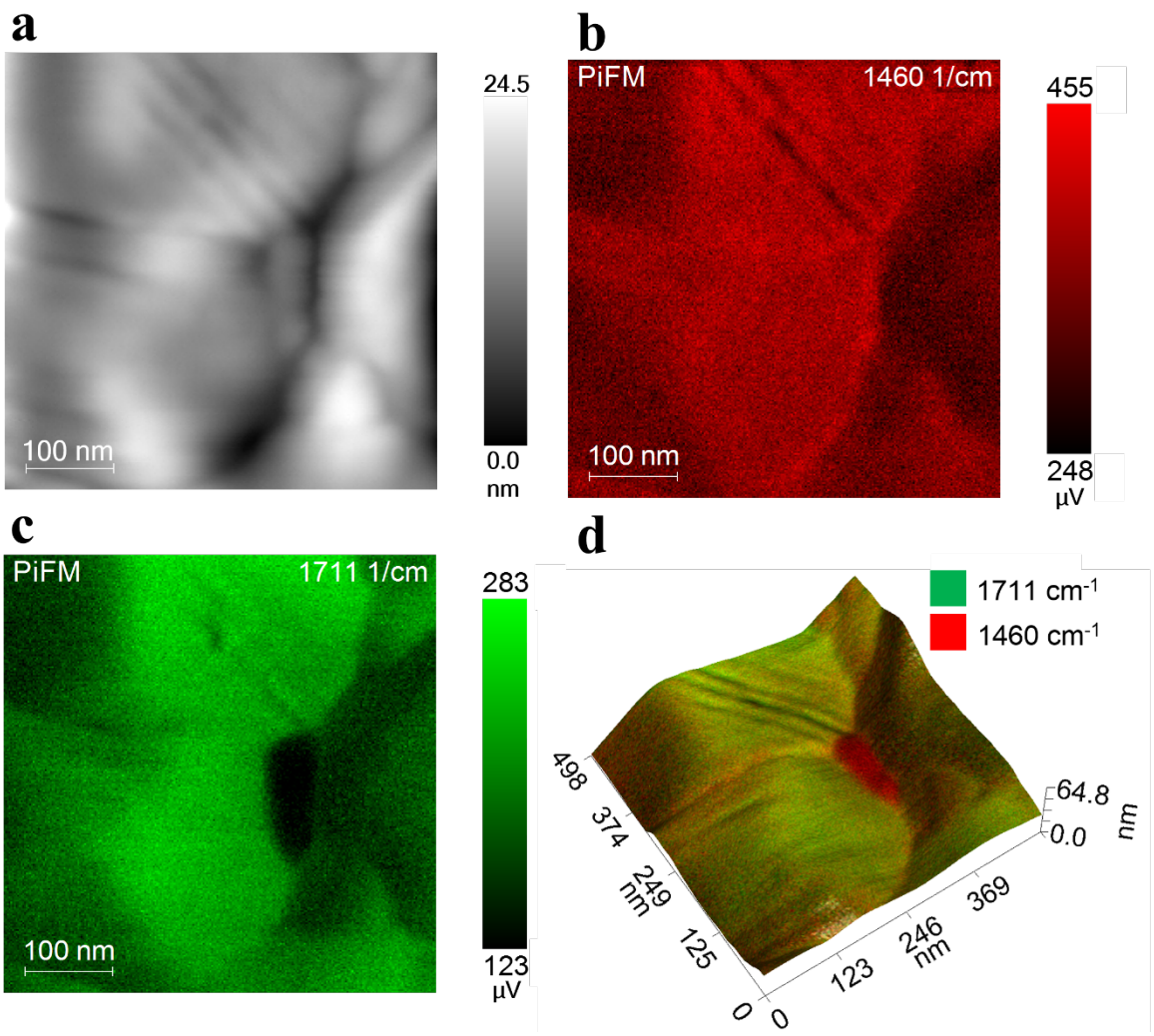

Fig. 2. Topography and PiFM imaging of $(FAPbI_3)_{0.85}(MAPbBr_3)_{0.15}$ perovskites. a. Topography map. PiFM maps at photo-induced force spectra of **b.** 1460 cm^{-1} (MA^+ molecule) and **c.** 1714 cm^{-1} (FA^+ molecule). **d.** A overlaid PiFM map at both wavenumbers (1460 cm^{-1} and 1714 cm^{-1}) on a 3D topography image.

Next, we evaluate the chemical composition of the domain structure using PiFM[37]. In PiFM, the sample's response to mid-IR radiation is recorded within the optical near-field of a scattering AFM tip. This technique allows mapping of infrared spectroscopic fingerprints revealing the sample's local chemical composition with few nanometer lateral resolution. The photo-induced force spectra of the $(FAPbI_3)_{0.85}(MAPbBr_3)_{0.15}$ films are measured at different

spots as shown in Fig. S2. The laser used for the PiFM measurements was a quantum cascade laser (QCL) with a range of 770-1890 cm^{-1} with an intensity range of 0.1-0.5 mW. Two peaks at 1470 cm^{-1} (symmetric NH_3^+ bend) and 1714 cm^{-1} (C-N antisymmetric stretching) are visible, which corresponds to MA^+ and FA^+ cation molecules, respectively.[38, 39] We confirm that there is no variation in the peak positions across different spots (Fig. S2c) but there are relative intensity variations. For example, a relatively much higher intensity of the FA^+ related peak (1714 cm^{-1}), above 1.4 mV, is attributed to higher amount of FA^+ molecules compared to the MA^+ peak (1470 cm^{-1}) with an intensity below 0.2 mV. Fig. 2 displays the AFM topography and the corresponding PiFM spatial maps, revealing the domain structures. As can be seen, the domain pattern with HTDs and LTDs is clearly visible in topography (Fig. 2a). The corresponding PiFM maps at 1460 cm^{-1} and 1714 cm^{-1} are displayed in Fig. 2b and 2c respectively. It can be seen that the domain pattern consists of alternating low and high intensities in both maps. This implies that there is a compositional variation across the domains. Particularly, a relatively stronger contrast variation is clearer in the 1460 cm^{-1} map than in the 1714 cm^{-1} map. Fig. 2d shows a 3D overlaid map with combined PiFM maps at both wavenumbers with topography. As can be seen, both red (1460 cm^{-1}) and green (1714 cm^{-1}) contrasts are significantly lower at the LTDs, indicating a deficiency of both FA and MA cations. Such alternating low and high domains could be responsible for a local distortion of the crystal lattice due to the A site deficiency, e.g., MA cation,[40] and twin domains with different crystal facets[40].

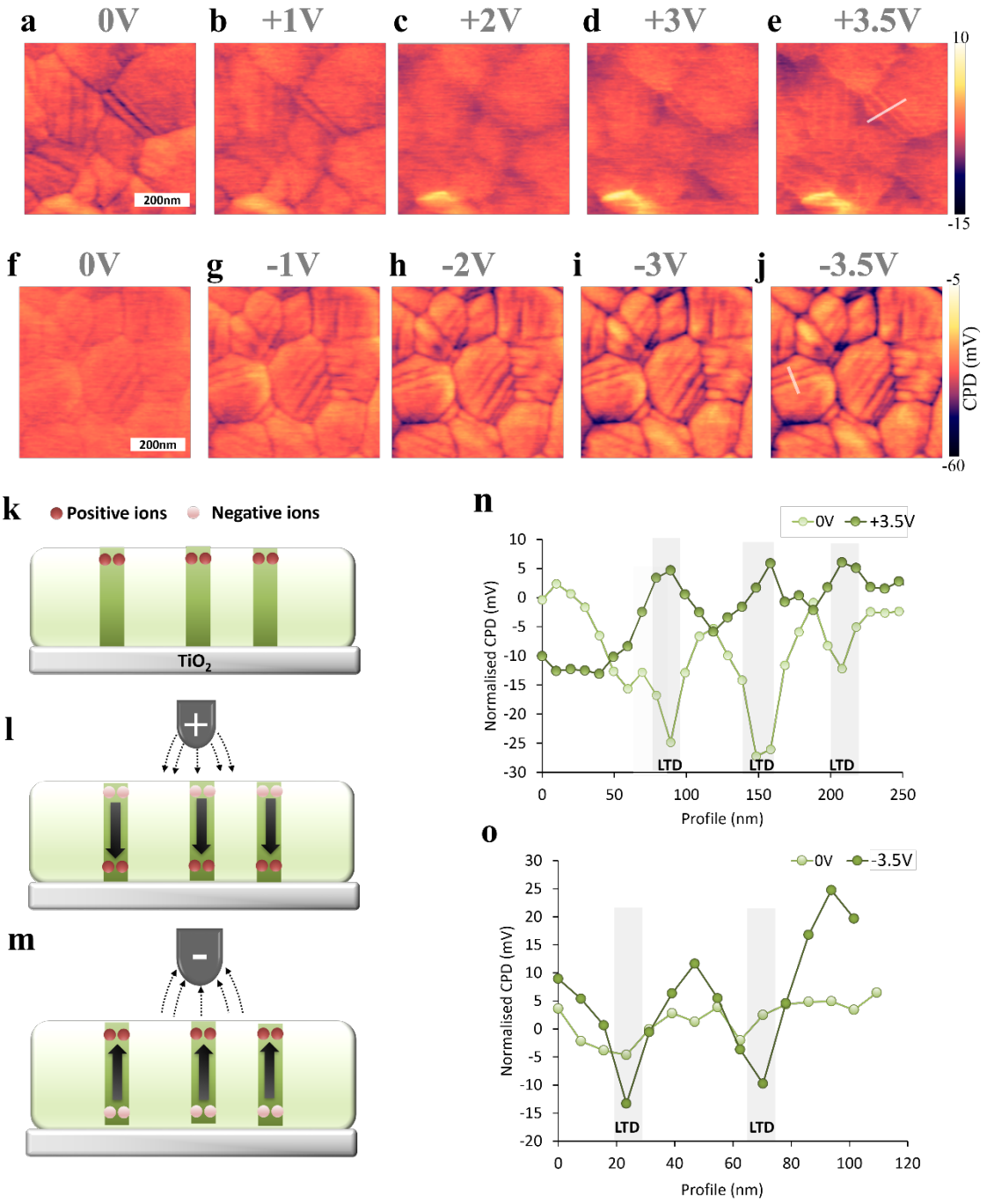

Fig. 3. DC bias electric field-driven ion migration observed in KPFM measurements. a-e. Normalized CPD spatial maps when a positive bias voltage (BV) is applied to the tip with different biases and **f-j.** a negative BV is applied to the tip with different biases. Schematic illustration of positive ions (organic cations) at LTDs under **k.** built-in electric field (equilibrium), **l.** positive BV applied tip, and **m.** negative BV applied tip. CPD profiles across LTDs with 0V and **n.** +3.5V **o.** -3.5V. The profiles are taken from the white lines in (e) (+3.5V) and (j) (-3.5V).

In order to observe ionic motion in the twin domain system under the influence of an electric field, we performed two-pass KPFM with varying bias voltages (BVs), the detailed

experimental setup is shown in Fig. S3. Fig. 3 shows a series of contact potential difference (CPD) maps at different external BVs. When there is no BV (0V), alternating LTDs and HTDs are visible with high and low CPD contrast that follows the domain pattern, as shown in Fig 3a and f. Line profiles of topography and CPD maps are displayed in Fig. S4. Here, we use a gold tip (work function Φ_{gold}= 5.1eV), therefore, the lower CPD at LTDs indicates that work function of the LTDs is relatively closer to the Φ_{gold} as the CPD corresponds to a work function difference between the tip (Φ_{tip}) and sample (Φ_{sample}). This observation can be linked with above PiFM results that suggests segregation of the cation vacancies at the LTDs. Cation vacancies create energy levels close to the valance band[15, 41, 42], resulting in lowering of the Fermi energy level, thus cation vacancies are pushed towards the surface by the built-in potential.

Fig. 3a-j display an evolution of CPD spatial maps when electric field is established toward the sample surface with positive (Figure 3l) and negative (Fig. 3m) BVs applied to the tip. As the positive bias increases from 0 to +3.5V (Fig. 3a-e), the overall CPD increases as the positive polarity attracts the negative ions such as halides, or positive ions such as cations are away from the surface. Interestingly, the CPD of the LTDs increases predominantly compared to the HTDs, clearly showing bright contrast as the BV increases. Conversely, when the potential direction is reversed (Fig. 3f-j), the CPD values at the LTDs become gradually lower compared to the HTDs. Fig. 3n and 3o present the CPD line profiles across the LTDs with positive and negative ±3.5V, respectively. At 0V, LTDs have lower CPD compared to the adjacent HTDs and this is completely reversed when positive +3.5V is applied to the tip as a result of predominant migration of cation vacancies towards a TiO_2 layer that increases CPD as shown in Fig. 3n. An exactly opposite phenomenon occurs when applying -3.5V, exhibiting a decrease in CPD at the LTDs due to attracting the cation vacancies towards the tip. Also, it is noteworthy to mention that the CPD variation across the LTDs does not have pronounced broader widths after applying both BVs, implying that the ion migration occurs like a confined tunnel within the LTDs. In other words, nearby mobile ions do not preferentially migrate to the LTDs, for instance, there is no lateral migration of the ions towards the LTDs.

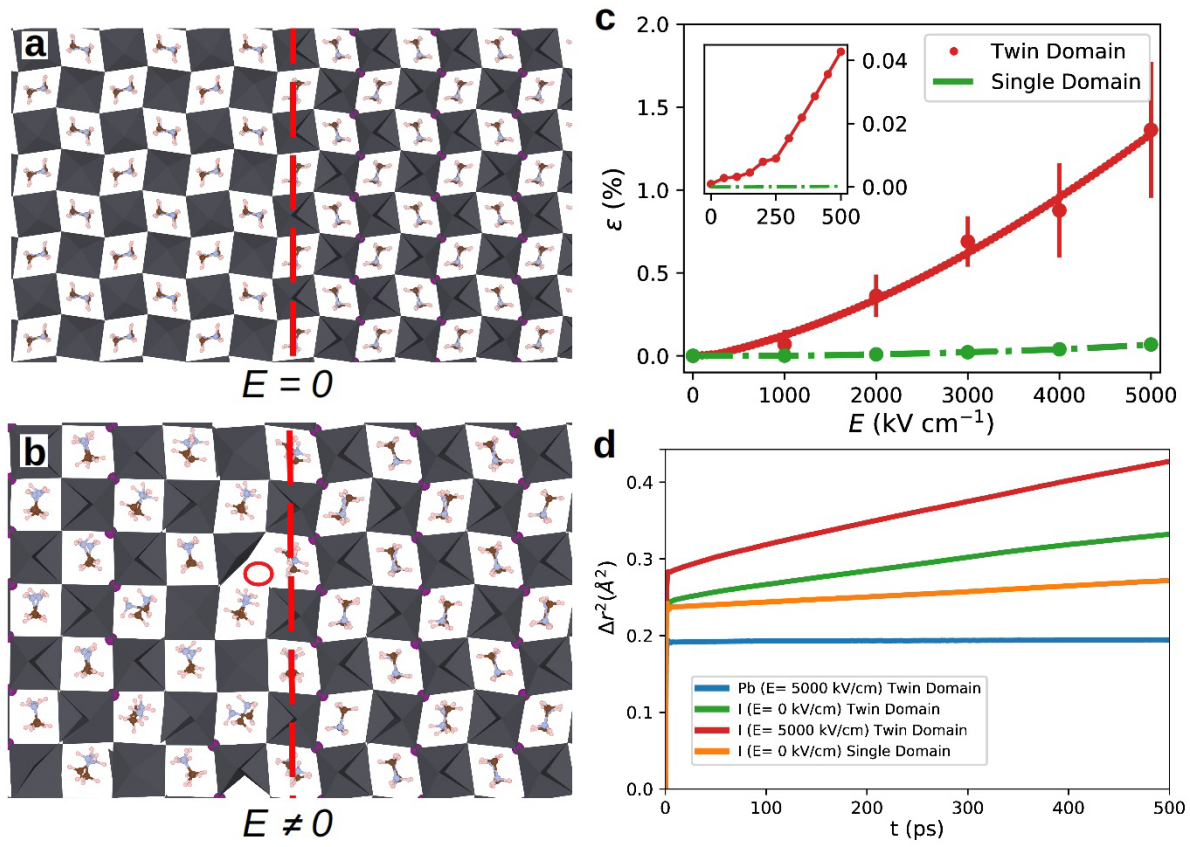

Fig. 4. Field-induced ion migration and lattice distortion at ferroelastic twin domains. a. Sketch of the initial ferroelastic twin-domain structure considered in MD simulations in the absence of an electric field; the approximate location of the TW is indicated with a red line. **b.** Sketch of the ferroelastic twin domain structure when an external electric field is applied to the system; the approximate location of an iodine vacancy is indicated with a red circle. **c.** Field-induced strain along the electric field direction calculated for a single domain and ferroelastic twin-domain system where the inset represents the enlarged area at lower electric fields **d.** Mean-squared displacement calculated at $T = 300$ K for a single domain and ferroelastic twin-domain system under the action and absence of an electric field.

To elucidate the enhanced ion migration in the domain system through the LTDs, we performed molecular dynamic (MD) simulations. In addition to the ion migration activation energy, structural variations must be taken into account when contemplating ion migration.[43, 44] Therefore, our MD simulations focus to reveal further atomistic insight into the structure of OHP ferroelastic twin domains and to understand the microscopic mechanisms sustaining ion migration within them based on the previously reported and successfully tested MYP force field.[45, 46]

Initially, we generated a 90° ferroelastic twin domain geometry based on the low-temperature (low-T) orthorhombic phase (non-polar, space group *Pnma*) of bulk OHPs, in which the iodide octahedral rotations follow the $a^-a^-a^+$ pattern in Glazer notation and the organic molecules MA remain orientationally ordered (Fig. 4a). We should note that it is not

possible to construct an analogous ferroelastic twin domain system based on the high-T cubic phase of bulk OHPs, due to the lack of order-parameter anisotropies. On the other hand, the employed MYP force field is tested to the LTDs to underestimate the c/a ratio of the tetragonal phase, thus we consider here the orthorhombic symmetry. The technical details of our twin domain simulations considering finite temperatures and electric fields can be found in the Methods section.

Under application of an external electric field, important structural and ion-transport differences appear between the ferroelastic twin and single domain systems (Fig. 4b-c). It is found that the single domain remains largely unresponsive to the electric bias (as it was expected owing to the non-polar nature of the orthorhombic *Pnma* phase), whereas the ferroelastic twin domain undergoes a noticeable elongation that roughly increases with the square of the electric field modulus (particularly, as $\partial^2\varepsilon/\partial E^2 = +5.7$ cm^2 kV^{-2}). The cause of such a large field-induced elongation is the breaking of crystal symmetries at the ferroelastic domain wall (Fig. 4a-b), which makes the ferroelastic twin domain system locally non-centrosymmetric and therefore responsive to electric bias (we note that a similar local symmetry breaking effect has been reported recently for ferroelastic twin domains in the halide perovskite $CsPbBr_3$[47]). Besides elongation, the electric field induces other important structural distortions in the twin domain system like for instance alignment of most organic molecules and significant depletion of the I_6 octahedral rotations in one of the two ferroelastic domains (red circle in Fig. 4b).

The large field-induced lattice elongation found in the ferroelastic twin domain has crucial consequences for the ion-transport properties of the system. Fig. 4d shows the mean-squared displacement of iodide and lead atoms, Δr^2, calculated at T = 300 K in the single domain and ferroelastic twin domain systems considering the presence and absence of electric fields (in the single domain system, we do not find any significant difference between zero and finite electric fields, hence we only report the $E = 0$ case, the slope of Δr^2 calculated at longer time is proportional to the diffusion coefficient of the corresponding ions, D (Methods). In our MD simulations, we only observe diffusion of the iodide ions (Fig. 4d) which was reported to be the dominant migrating ion species with the largest diffusion coefficient.[48] At room temperature, the diffusivity of the I atoms in the single domain system is equal to $1.28 \cdot 10^{-6}$ cm^2/s. At zero electric field, the T = 300 K diffusivity of the iodide ions in the ferroelastic twin domain system already increases by a factor of 2.4 as compared to the single domain case. The reason for such an increase in D is due to a reduction in the crystal symmetry and appearance of a strain field caused by the presence of the twin-domain wall. We should note that in our simulations ionic diffusion occurs homogeneously rather than in a concentrated area around the TW (Supplementary Fig. S5). However, due to the limitation in the number of atoms that we can simulate, the width of the simulated twin domains is quite small, *i.e.*, only a few nanometers. Interestingly, when a large electric field bias of 5,000 kV/cm is applied in the direction parallel to the TW, the ferroelastic twin domain stretches significantly along the same direction and the diffusion coefficient of the iodide atoms increases up to $4.55 \cdot 10^{-6}$ cm^2/s. This latter value is about 62% larger than estimated in the same system at $E = 0$. The main reason for such a huge room-temperature increase in D is the large field-induced elongation

experienced by the lattice, an effect somehow equivalent to applying a positive uniaxial stress[49] that makes the volume available to the interstitials to increase noticeably (in fact, the diffusion coefficient of the I ions along the electric field direction turns out to be 38% larger than calculated in the perpendicular direction, Supplementary Fig. S5). By contrast, application of the same electric field bias in the single domain system has a negligible effect both on the lattice dimensions and diffusion of the iodide ions. We argue, therefore, that the observed electric field-driven enhancement of I diffusivity in the ferroelastic twin domain system is lattice mediated and originally caused by the breaking of crystal symmetries at the TW.

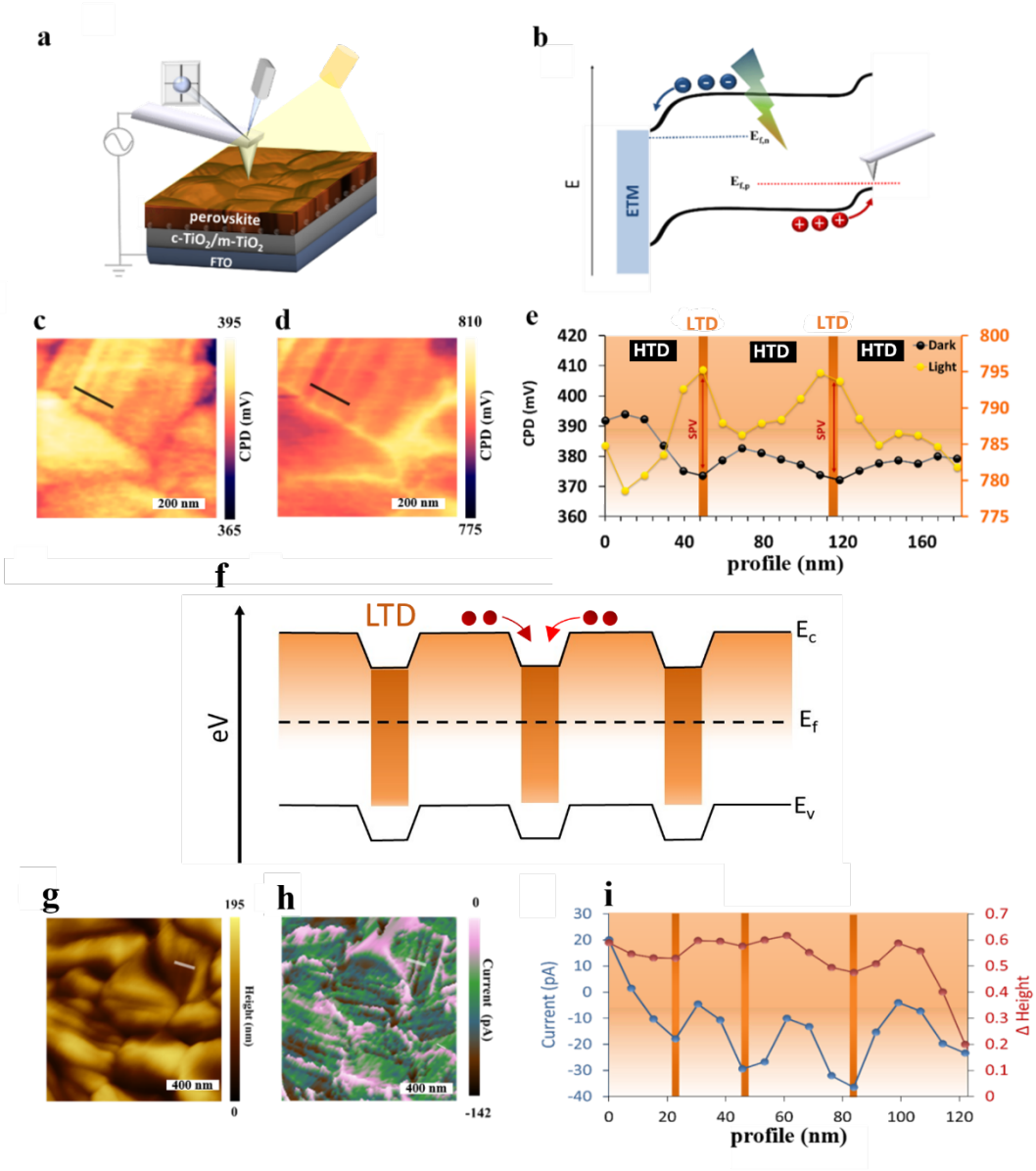

Fig. 5. Surface photovoltage and photocurrent maps. a. Schematic illustration of KPFM experimental setup on perovskite layers under illumination. **b.** Band diagram for an illuminated perovskites with the cantilever where $E_{f,n}$ and $E_{f,p}$ are the electron and hole quasi-Fermi levels, respectively. CPD spatial maps in **c.** dark and **d.** under illumination. **e.** CPD profiles of HTDs and LTDs in dark and light (black line in c-d). **f.** Topography and **g.** the corresponding photocurrent map. **h.** Line profile of current and height of the white line in f-g. **i.** Schematic illustration of band structure of LTDs and HTDs.

To obtain insight into charge separation properties of the twin domain system, we performed KPFM under illumination (white LED and intensity of 0.3W/cm^2) which allows extraction of the local surface photovoltage. Fig. 5a shows an illustration of light-assisted KPFM experimental setup. The band diagram of a perovskite layer with a metal AFM tip under illumination is illustrated in Fig. 5b. The hole quasi-Fermi level of the perovskite and the tip is assumed to be in equilibrium, enabling determination of the quasi-Fermi split to be probed via the tip under illumination. Fig. 5c-d shows spatial CPD maps of a domain that consists of both

LTDs and HTDs in dark and light, respectively. Overall CPD distribution in dark and light is displayed in Fig. S6 which shows an increase in CPD upon light illumination due to the hole accumulation at the top surface. In the absence of free charge carriers (dark condition), LTDs have lower CPD compared to HTDs as discussed in Fig. 3. Upon illumination, the CPD at LTDs becomes relatively higher compared to the HTDs. Surface photovoltage (CPD measured in light deduced from CPD measured in dark) of the LTDs is plotted in orange-coloured bars in Fig. 5e, which clearly indicates that the LTDs have higher surface photovoltage. This suggests that more charge carriers have been separated around the LTDs compared to the HTDs. We speculate that more positively charged LTDs promote downward band bending towards the LTDs and facilitates efficient charge separation as illustrated in Figure 5f.

To further verify the charge transport properties of the domain structure, we performed c-AFM measurements under illumination. Unlike KPFM which employs a non-contact mode, the sample surface is in contact with the AFM tip in c-AFM set-up. In principle, the charge carriers that are generated and separated at the TiO_2/perovskite interface can drift (*i.e.*, a current flows) and can be collected by a gold-coated AFM tip. In this configuration, electrons are collected at the contact of the FTO and holes are collected by the AFM tip which is illustrated in Fig. S7a. Using this technique, spatial photocurrent maps are obtained. A typical intensity dependent *I-V* curve measured by the c-AFM setup is shown in Fig. S7b where more negative currents are detected upon a higher intensity of light illumination. Fig. 5g-h shows a topography map and the corresponding photocurrent map. In the topography map, domain patterns within grains can be observed and the photocurrent map exhibits clear difference between LTDs and HTDs. Fig. 5i shows the profiles of the current and height change in white lines drawn in Fig. 5g-h. As can be seen, negatively higher current areas coincide with lower topography, which implies that the charge collection is higher at the LTDs compared to the HTDs. It is interesting to note that the GBs exhibit almost no photocurrent compared to inner grains or domains. From our previous work on the single composition $MAPbI_3$ perovskite, we observed that both SPV and photocurrent were higher at the GBs.[21] The mixed composition in this work would have non-uniform distribution of both cations and halides that results in bandgap fluctuation.[50, 51] One possibility is that GBs have larger bandgap due to Br segregation that locally enlarges the bandgap and results in higher SPV with lower photocurrent. While the mixed composition OHPs possess a variety of advantages such as tuning of bandgap and optical properties, our results clearly suggest that both structural and compositional heterogeneity exist, which can limit the device performance. This could be improved by domain engineering due to the better charge carrier transport properties of such domains.

Conclusions

In summary, we have successfully visualized ferroelastic twin domains in mixed halide perovskites using AFM topography image and PFM amplitude response, as well as photo-induced force microscopy. While grain boundaries in halide perovskites are known to be a predominant channel for ion migration, our result reveals that the domain system also provides a confined preferential tunnel for the ion migration. The observed domains include narrow

(lower height) and wide domains (higher height) that exist alternately. We further investigate the chemical composition of the domain structure using PiFM. Our results reveal an alternating segregation of FA and MA cations along with the domain structures. In addition, KPFM measurements in dark reveal that the CPD values are alternating along LTDs (lower CPD) and HTDs (higher CPD), as consequences of structural and chemical difference between the domains. BV-dependent KPFM images show that LTDs act as a migration tunnel for the mobile ions. MD simulations suggest that the origin of such an electric field enhancement of the ionic conductivity is related to the centrosymmetry breaking at the twin domain walls, which makes the system locally piezoelectric and consequently mechanically susceptible and responsive to electric bias. In turn, the resulting electric field induced stretching of the perovskite lattice facilitates the diffusion of mobile ions. Importantly, our photovoltage maps reveal that the SPV is relatively higher at the LTDs as compared to HTDs. Also, photocurrent maps using c-AFM confirm that the photocurrent is exceptionally higher at these LTDs compared to grain boundaries. Our study suggests that efficient charge separation and collection at LTDs can contribute to enhanced device performance. We believe that our observations will rouse up the engineering of controlled domain properties to improve perovskite solar cell performance.

Acknowledgements

A.M. acknowledges Italian MIUR for funding through project PON04a2_00490 M2M Netergit and PRACE for awarding access to Marconi KNL at CINECA, Italy, through projects DECONVOLVES (2018184466) and PROVING-IL (2019204911). J.S. and P.S. acknowledge support by the ARC Centre of Excellence in Future Low Energy Electronics Technology (FLEET). D.K. acknowledges support from the Korea Institute of Energy Technology Evaluation and Planning (KETEP).

Experimental Methods

Materials

All chemicals were purchased from Sigma-Aldrich, Alfa Aesar and Lumtec (Luminescence Technology Corp.) and used without further purification. $HC(NH_2)_2I$ were synthesized by reacting 15 g formamidine acetate and 30 ml HI (57 wt% in water) in 100 ml ethanol at 0 °C for 2 hours with stirring. The precipitate was recovered by using a rotary evaporator at 50 °C for 1 hour. White crystals were obtained by washing with diethyl ether followed by recrystallization with ethanol. CH_3NH_3Br wes synthesized by reacting 11 ml methylamine solution (33 wt% in water) and 10 ml HBr (48 wt% in water) in 100 ml ethanol at 0 °C for 2 hours with stirring. The precipitate was recovered by using a rotary evaporator at 50 °C for 1 hour. White crystals were obtained by washing with diethyl ether followed by recrystallization with ethanol.

To prepare 1.2M $HC(NH_2)_2PbI_3$ (or $CH_3NH_3Br_3$) solution, the prepared $HC(NH_2)_2I$ (or CH_3NH_3Br) was mixed with PbI_2 (or $PbBr_2$) in dimethylformamide (DMF):dimethyl sulfoxide (DMSO) mixed solvent (1:0, 1:0.25, or 1:0.17 volume ratio) at room temperature. For the solution of $(HC(NH_2)_2PbI_3)_{0.85}(CH_3NH_3PbBr_3)_{0.15}$, prepared $HC(NH_2)_2PbI_3$ and $CH_3NH_3Br_3$ solution are mixed with the corresponding volume ratio. For the perovskite solution used for this study, extra PbI_2 (5 mol% to $HC(NH_2)_2PbI_3$) was mixed with the prepared $(HC(NH_2)_2PbI_3)_{0.85}(CH_3NH_3PbBr_3)_{0.15}$ solution and heated at 60 °C for 30 mins.

Solar Cell Fabrication

A dense blocking layer of TiO_2 (bl-TiO_2) was deposited by spray pyrolysis using 20 mM titanium diisopropoxide bis(acetylacetonate) solution at 450 °C on the clean FTO glass (TEC8) with metal grid for large area device. On top of the bl-TiO_2 layer, 150 mg ml^{-1} of mesoporous TiO_2 paste (m-TiO_2, Dyesol 30 NR-D) in ethanol was spin-coated at 5000rpm (acceleration of 2000 rpm s^{-1}) for 10 sec. Then, the substrates were annealed at 100 °C for 10 mins followed by sintering at 500 °C for 30 mins.

The prepared perovskite solution was spun at 2000 rpm (acceleration of 200 rpm s^{-1}) and 6000 rpm (acceleration of 2000 rpm s^{-1}) for 10 sec and 30 sec, respectively. During the last 20 sec of the second spin-coating step, the anti-solvent chlorobenzene was drop-casted (110 µL or 688 µL). The perovskite film was dried on a hot plate at 100 °C for 20 min. A solution of Spiro-OMeTAD containing 72.3 mg Spiro-OMeTAD, 17.5 µl of a 520 mg ml^{-1} lithium bis (trifluoro-methylsulphonyl)imide in acetonitrile and 31.2 µl of 4-tert-butylpyridine in 1 ml chlorobenzene was spin-coated on the perovskite/m-TiO_2/bl-TiO_2/FTO substrate at 2000 rpm (acceleration of 1200 rpm s^{-1}) for 20 s. All films on m-TiO_2 were prepared in a nitrogen filled glovebox. A gold electrode was deposited by thermal evaporation.

Characterization methods

The PFM measurements were performed using a commercial AFM system (AIST-NT SmartSPM 1000) under ambient conditions at room temperature. Nitrogen gas was used for cleaning sample surfaces before measurements. PFM images were taken on the surface of the

films after they were cleaned with nitrogen gas using Pt-coated (HQ:CSC 37/PT, μmasch, force constant, k = 0.8 N/m) Si cantilevers that possesses a range of resonance frequencies from 30 to 55kHz for AFM and PFM. AC bias (1500~2000mV) was applied to the PFM tips, the lowest one among the resonance peaks was chosen. All PFM data was obtained with out-of-plane and in-plane amplitude and phase maps at the same scan. Light sources were blocked for dark conditions. Tuneable white LED light sources that are not filtered were used for illumination at an intensity of 0.3-0.5 W/cm^2. DC bias was applied towards the tip or sample. c-AFM and KPFM measurements were carried out using diamond-coated conductive probes (DCP20, force constant, k= 48 N/m) possessing a resonance frequency of 420 kHz or gold-coated conductive probes (HQ:NSC36/CR-AU, force constant, k=1 N/m) possessing a resonance frequency of 90 kHz . A scan rate of 1Hz is used with 256 x 256 pixels.

X-ray diffraction (XRD) patterns were measured using a PANalytical Xpert Materials Research diffractometer system with Cu Kα radiation source (λ = 0.1541 nm) at 45 kV and 40 mA.

The J–V measurements were performed using a solar cell I–V testing system from Abet Technologies, Inc. (using class AAA solar simulator and Keithley 2400 source meter) under an illumination power of 100 mW cm^{-2} with an 0.03 cm^2.

MD simulations

MD (MD) simulations were performed in the (*N*,*P*,*T*) and (*N*,*V*,*T*) ensembles with the LAMMPS code.[52] The pressure and temperature in the system were kept fluctuating around a set-point value by using thermostatting and barostatting techniques in which some dynamic variables are coupled to the particle velocities and simulation box dimensions. The interactions between ions were modelled with the MYP classical interatomic potential recently developed by Mattoni and co-workers.[45, 46] We employ a large simulation box containing 92,256 atoms (equivalent to 7,688 $CH_3NH_3PbI_3$ formula units), and apply periodic boundary conditions along the three Cartesian directions. Without any loss of generality, the dimensions of the simulation supercell containing the initial 90^o ferroelastic TD geometry are equal to 547.351 Å x 270.526 Å x 12.37 Å, with the domain wall oriented along the Cartesian direction y = [010]; in this way, the size of the ferroelastic domains along one direction perpendicular to their boundary can be made reasonably large while keeping the computational cost of the accompanying simulations within affordable limits.

Newton's equations of motion were integrated by using the customary Verlet algorithm with a time-step length of 1 fs. The typical duration of a MD run was of 1,000 ps. A particle–particle particle–mesh k-space solver was used to compute long-range Van der Waals and Coulomb interactions beyond a cut-off distance of 12 Å at each time step. For the calculation of ionic diffusion coefficients at T = 300 K, we introduced a 1% concentration of iodine vacancies randomly distributed within the system.

To analyse the superionic transport properties of $CH_3NH_3PbI_3$, we computed the corresponding diffusion coefficient, D, and mean-squared displacement, $\Delta r^2(t)$. The diffusion coefficient is defined as:

$$D = \lim_{t\to\infty} \frac{\langle |r_i(t+t_o) - r_i(t_o)|^2 \rangle}{6t},$$

where $r_i(t)$is the position of the migrating ion labeled as $i$at time t, t_0, an arbitrary time origin, and $\langle \ldots \rangle$ denotes average over time origins and particles.[53] Meanwhile, the mean-squared displacement of each ionic species is defined as:

$$\langle \Delta r_i^2(t) \rangle = \langle |r_i(t + t_o) - r_i(t_0)|^2 \rangle .$$

In our MD simulations, the orthorhomic *Pnma* phase transitates to a tetragonal *I4/mcm* phase at a temperature close to 150 K. [43] When this transition occurs, the twin domain boundary disappears from the system. Consequently, it is not possible to study the ionic diffusion properties of the 90º ferroelastic TD system at room temperature (neither of the orthorhombic SD system). In order to avoid the disappearance of the twin domain wall from the system, we first performed (*N*,*P*,*T*) simulations at a safely low temperature of 50 K, considering either null or finite electric fields; subsequently, we fixed the positions of the organic molecules and the volume of the system, *V*, and increased the temperature all the way up to room temperature. The iodine and lead ions were set free to move at all times and temperatures. In this way, we were able to constrain the presence of the twin domain wall in our room-temperature MD simulations.

References

1. Jeon NJ*, et al.* Compositional engineering of perovskite materials for high-performance solar cells. *Nature* **517**, 476 (2015).

2. Liu M, Johnston MB, Snaith HJ. Efficient planar heterojunction perovskite solar cells by vapour deposition. *Nature* **501**, 395 (2013).

3. Dou L*, et al.* Solution-processed hybrid perovskite photodetectors with high detectivity. *Nature communications* **5**, 5404 (2014).

4. Fang Y, Dong Q, Shao Y, Yuan Y, Huang J. Highly narrowband perovskite single-crystal photodetectors enabled by surface-charge recombination. *Nature Photonics* **9**, 679 (2015).

5. Sutherland BR, Sargent EH. Perovskite photonic sources. *Nature Photonics* **10**, 295 (2016).

6. Green MA, Dunlop ED, Levi DH, Hohl-Ebinger J, Yoshita M, Ho-Baillie AW. Solar cell efficiency tables (version 54). *Progress in Photovoltaics: Research and Applications* **27**, 565-575 (2019).

7. Stranks SD*, et al.* Electron-hole diffusion lengths exceeding 1 micrometer in an organometal trihalide perovskite absorber. *Science* **342**, 341-344 (2013).

8. Mitzi DB, Feild C, Schlesinger Z, Laibowitz R. Transport, optical, and magnetic properties of the conducting halide perovskite CH3NH3SnI3. *Journal of Solid State Chemistry* **114**, 159-163 (1995).

9. Kojima A, Teshima K, Shirai Y, Miyasaka T. Organometal Halide Perovskites as Visible-Light Sensitizers for Photovoltaic Cells. *Journal of the American Chemical Society* **131**, 6050-6051 (2009).

10. Noh JH, Im SH, Heo JH, Mandal TN, Seok SI. Chemical management for colorful, efficient, and stable inorganic–organic hybrid nanostructured solar cells. *Nano letters* **13**, 1764-1769 (2013).

11. Steirer KX*, et al.* Defect tolerance in methylammonium lead triiodide perovskite. *ACS Energy Letters* **1**, 360-366 (2016).

12. Leblebici SY*, et al.* Facet-dependent photovoltaic efficiency variations in single grains of hybrid halide perovskite. *Nature Energy* **1**, 16093 (2016).

13. Kim D*, et al.* Light-and bias-induced structural variations in metal halide perovskites. **10**, 1-9 (2019).

14. Gratia P*, et al.* Intrinsic halide segregation at nanometer scale determines the high efficiency of mixed cation/mixed halide perovskite solar cells. *Journal of the American Chemical Society* **138**, 15821-15824 (2016).

15. Yun JS*, et al.* Critical role of grain boundaries for ion migration in formamidinium and methylammonium lead halide perovskite solar cells. *Advanced Energy Materials* **6**, 1600330 (2016).

16. Shao Y*, et al.* Grain boundary dominated ion migration in polycrystalline organic–inorganic halide perovskite films. *Energy & Environmental Science* **9**, 1752-1759 (2016).

17. Jones TW*, et al.* Lattice strain causes non-radiative losses in halide perovskites. *Energy & Environmental Science* **12**, 596-606 (2019).

18. Chen B*, et al.* Perovskite Solar Cells: Imaging Spatial Variations of Optical Bandgaps in Perovskite Solar Cells (Adv. Energy Mater. 7/2019). *Advanced Energy Materials* **9**, 1970021 (2019).

19. Heo S*, et al.* Deep level trapped defect analysis in CH 3 NH 3 PbI 3 perovskite solar cells by deep level transient spectroscopy. **10**, 1128-1133 (2017).

20. Zheng X*, et al.* Defect passivation in hybrid perovskite solar cells using quaternary ammonium halide anions and cations. **2**, 1-9 (2017).

21. Yun JS*, et al.* Benefit of grain boundaries in organic–inorganic halide planar perovskite solar cells. *The journal of physical chemistry letters* **6**, 875-880 (2015).

22. Lee J-W, Bae S-H, De Marco N, Hsieh Y-T, Dai Z, Yang YJMTE. The role of grain boundaries in perovskite solar cells. **7**, 149-160 (2018).

23. Yuan Y, Huang J. Ion migration in organometal trihalide perovskite and its impact on photovoltaic efficiency and stability. *Accounts of Chemical Research* **49**, 286-293 (2016).

24. Liu Y*, et al.* Chemical nature of ferroelastic twin domains in CH 3 NH 3 PbI 3 perovskite. *Nature materials* **17**, 1013 (2018).

25. Rothmann MU*, et al.* Direct observation of intrinsic twin domains in tetragonal CH 3 NH 3 PbI 3. *Nature communications* **8**, 14547 (2017).

26. Hermes IM*, et al.* Ferroelastic fingerprints in methylammonium lead iodide perovskite. *The Journal of Physical Chemistry C* **120**, 5724-5731 (2016).

27. Strelcov E*, et al.* CH3NH3PbI3 perovskites: Ferroelasticity revealed. *Science advances* **3**, e1602165 (2017).

28. Leonhard T*, et al.* Probing the Microstructure of Methylammonium Lead Iodide Perovskite Solar Cells. *Energy Technology*, (2019).

29. Röhm H, Leonhard T, Hoffmann MJ, Colsmann A. Ferroelectric domains in methylammonium lead iodide perovskite thin-films. *Energy & Environmental Science* **10**, 950-955 (2017).

30. Ramirez C, Yadavalli SK, Garces HF, Zhou Y, Padture NP. Thermo-mechanical behavior of organic-inorganic halide perovskites for solar cells. *Scripta Materialia* **150**, 36-41 (2018).

31. Xiao X*, et al.* Benign ferroelastic twin boundaries in halide perovskites for charge carrier transport and recombination. **11**, 1-7 (2020).

32. Liu Y*, et al.* Dynamic behavior of CH3NH3PbI3 perovskite twin domains. **113**, 072102 (2018).

33. Hermes IM*, et al.* Anisotropic carrier diffusion in single MAPbI3 grains correlates to their twin domains. *Energy & Environmental Science* **13**, 4168-4177 (2020).

34. Kim J*, et al.* Overcoming the challenges of large-area high-efficiency perovskite solar cells. *ACS Energy Letters* **2**, 1978-1984 (2017).

35. Kim D*, et al.* Light-and bias-induced structural variations in metal halide perovskites. **10**, 444 (2019).

36. Wondratschek H, Jeitschko W. Twin domains and antiphase domains. *Acta Crystallographica Section A: Crystal Physics, Diffraction, Theoretical and General Crystallography* **32**, 664-666 (1976).

37. Sifat AA, Jahng J, Potma EO. Photo-induced force microscopy (PiFM) – principles and implementations. *Chemical Society Reviews* **51**, 4208-4222 (2022).

38. Taylor VC*, et al.* Investigating the role of the organic cation in formamidinium lead iodide perovskite using ultrafast spectroscopy. **9**, 895-901 (2018).

39. Patel JB, Milot RL, Wright AD, Herz LM, Johnston MBJTjopcl. Formation dynamics of CH3NH3PbI3 perovskite following two-step layer deposition. **7**, 96-102 (2016).

40. Liu Y*, et al.* Chemical nature of ferroelastic twin domains in CH3NH3PbI3 perovskite. *Nature Materials* **17**, 1013-1019 (2018).

41. Yin W-J, Shi T, Yan Y. Unusual defect physics in CH3NH3PbI3 perovskite solar cell absorber. *Applied Physics Letters* **104**, 063903 (2014).

42. Kim J, Lee S-H, Lee JH, Hong K-H. The role of intrinsic defects in methylammonium lead iodide perovskite. *The journal of physical chemistry letters* **5**, 1312-1317 (2014).

43. Tan S*, et al.* Steric Impediment of Ion Migration Contributes to Improved Operational Stability of Perovskite Solar Cells. **32**, 1906995 (2020).

44. Cho J, DuBose JT, Le ANT, Kamat PVJAML. Suppressed Halide Ion Migration in 2D Lead Halide Perovskites. **2**, 565-570 (2020).

45. Mattoni A, Filippetti A, Saba M, Delugas PJTJoPCC. Methylammonium rotational dynamics in lead halide perovskite by classical molecular dynamics: the role of temperature. **119**, 17421-17428 (2015).

46. Delugas P, Caddeo C, Filippetti A, Mattoni AJTjopcl. Thermally activated point defect diffusion in methylammonium lead trihalide: anisotropic and ultrahigh mobility of iodine. **7**, 2356-2361 (2016).

47. Warwick AR, Íñiguez J, Haynes PD, Bristowe NCJTjopcl. First-principles study of ferroelastic twins in halide perovskites. **10**, 1416-1421 (2019).

48. Eames C, Frost JM, Barnes PR, O'regan BC, Walsh A, Islam MSJNc. Ionic transport in hybrid lead iodide perovskite solar cells. **6**, 7497 (2015).

49. Sagotra AK, Cazorla CJAam, interfaces. Stress-mediated enhancement of ionic conductivity in fast-ion conductors. **9**, 38773-38783 (2017).

50. Feldmann S*, et al.* Photodoping through local charge carrier accumulation in alloyed hybrid perovskites for highly efficient luminescence. **14**, 123-128 (2020).

51. Gratia P*, et al.* Intrinsic halide segregation at nanometer scale determines the high efficiency of mixed cation/mixed halide perovskite solar cells. **138**, 15821-15824 (2016).

52. Plimpton S. Fast parallel algorithms for short-range molecular dynamics.). Sandia National Labs., Albuquerque, NM (United States) (1993).

53. Sagotra AK, Chu D, Cazorla CJPRM. Influence of lattice dynamics on lithium-ion conductivity: A first-principles study. **3**, 035405 (2019).